Electronic Supplementary Material (ESI) for Journal of Materials Chemistry A.

Supporting Information for:

Electrochemically Synthesized Liquid-Sulfur/Sulfide Composite Materials for High-Rate Magnesium Battery Cathodes

Kohei Shimokawa,[1,2]* Takuya Furuhashi,[1] Tomoya Kawaguchi,[1] Won-Young Park,[1]
Takeshi Wada,[1] Hajime Matsumoto,[3] Hidemi Kato,[1] Tetsu Ichitsubo[1]*

[1]*Institute for Materials Research, Tohoku University, Sendai 980-8577, Japan*
[2]*Frontier Research Institute for Interdisciplinary Sciences, Tohoku University, Sendai 980-8578, Japan*
[3]*Research Institute of Electrochemical Energy, National Institute of Advanced Industrial Science and Technology (AIST), 1-8-31, Midorigaoka, Ikeda, Osaka 563-8577, Japan*

*E-mail: kohei.shimokawa.b7@tohoku.ac.jp; tichi@imr.tohoku.ac.jp

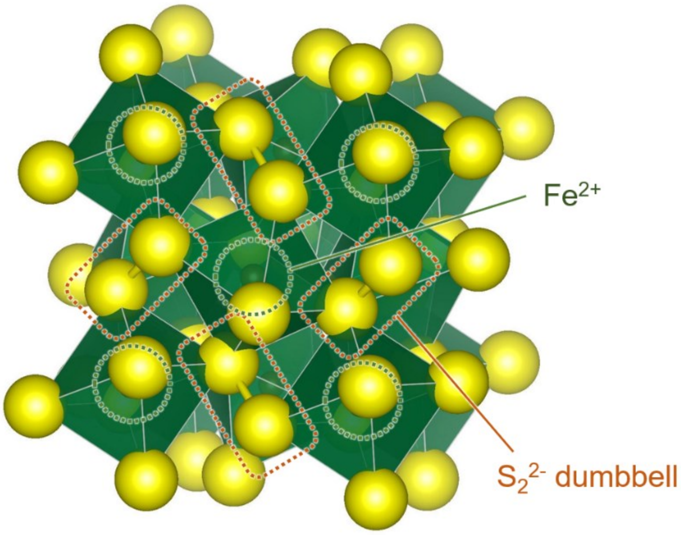

Figure S1. Schematic illustration showing the crystal structure of FeS_2 (i.e., pyrite structure). It can be seen as the rocksalt structure consisting of Fe^{2+} cations and S_2^{2-} dumbbell-shaped anions. The crystal structure was visualized using VESTA [S1].

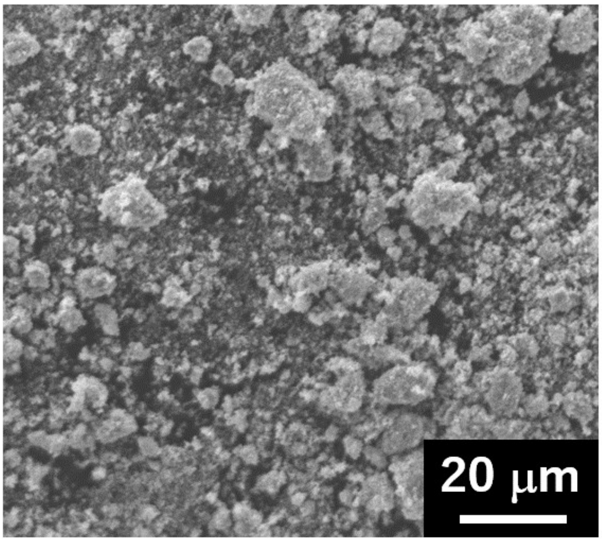

Figure S2. SEM image of FeS_2 powder used in preparing composite electrodes for electrochemical measurements. The particle size of FeS_2 powder was typically less than 20 μm.

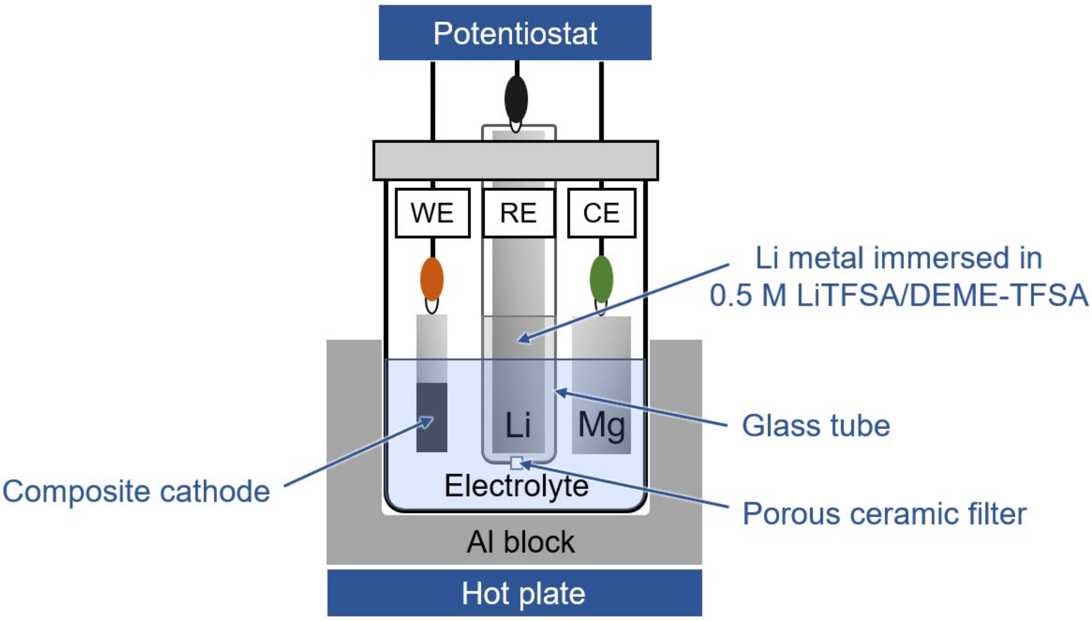

Figure S3. Schematic illustration of the beaker-type cell used for the electrochemical experiments. The temperature of the electrolyte was kept at 150℃ with an Al block heated by a hot plate. All electrochemical measurements were carried out in a glove box filled with Ar gas. Mg metal used for the counter electrode was polished with sandpaper inside the glove box prior to use. Li metal immersed in a solution of 0.5 M LiTFSA/DEME-TFSA was used for the reference electrode (denoted as Li RE), because Mg metal is readily passivated in TFSA based electrolytes. The Li-based solution is separated from the main bath by a grass tube with a porous ceramic filter to prevent the contamination of Li ions into the electrolyte.

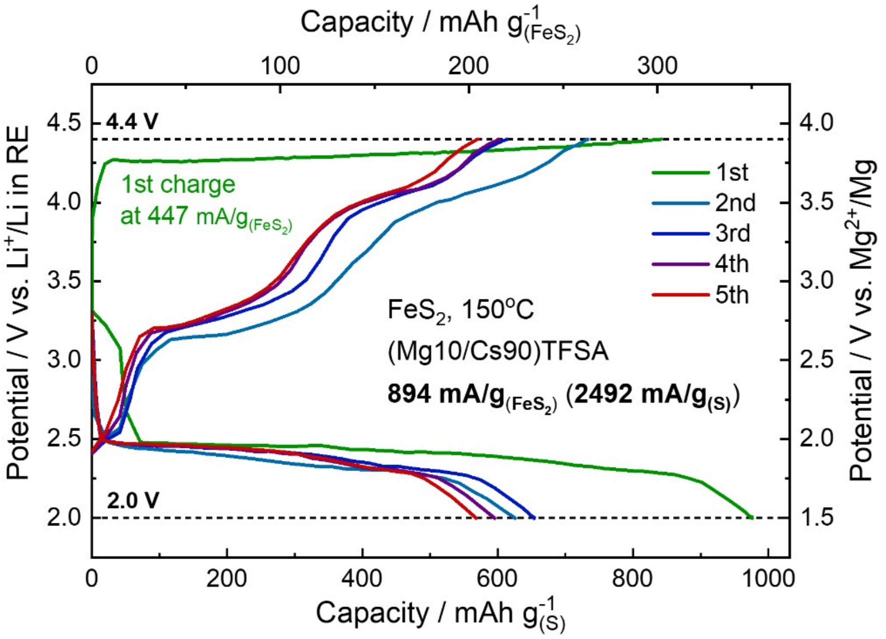

Figure S4. Charge/discharge curves of the S/FeS_2 cathode at a current density of 894 mA/$g_{(FeS2)}$ (i.e., 2492 mA/$g_{(S)}$), where the first charge was conducted for 300 mAh/$g_{(FeS2)}$ at 447 mA/$g_{(FeS2)}$. Although the decrease in capacity was observed after the first discharge, the cell stably showed discharge capacities of over 500 mAh/$g_{(S)}$ at 2492 mA/$g_{(S)}$ in the subsequent cycles on the basis of active S amount.

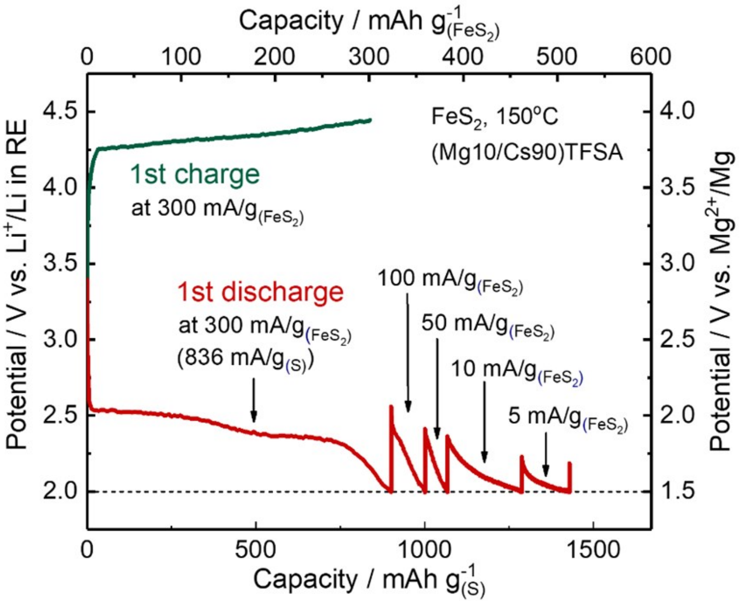

Figure S5. Discharge behavior of the S/FeS_2 cathode when the current density was decreased stepwise from 300 to 5 mA/$g_{(FeS2)}$, where the first charge capacity was 300 mAh/$g_{(FeS2)}$.

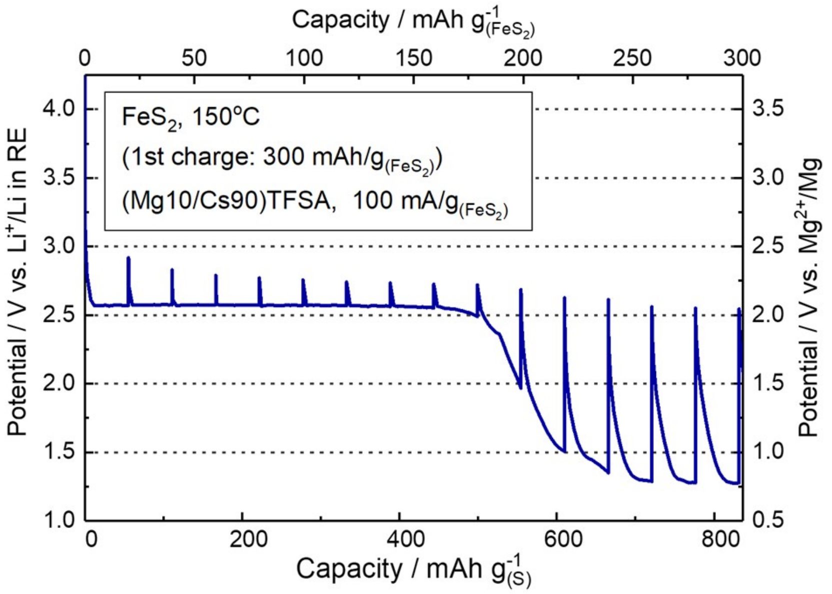

Figure S6. GITT profile of the S/FeS_2 cathode in the first discharging process after the first charge to 300 mAh/$g_{(FeS2)}$. The current density was set at 100 mA/$g_{(FeS2)}$. The rest time was defined as the time until the open circuit potential became stable (i.e., less than 30 mV/hour).

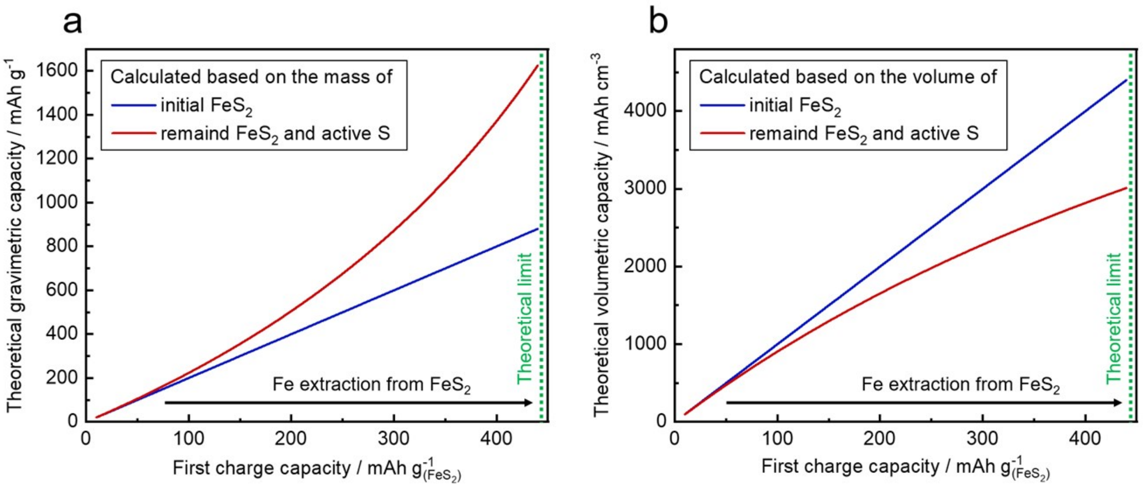

Figure S7. Theoretical (a) gravimetric and (b) volumetric capacities as a function of the first charge capacity (i.e., the amount of Fe extracted from FeS_2). The values based on the mass/volume of (i) initial FeS_2 and (ii) the sum of remained FeS_2 and active S are indicated by blue and red lines, respectively. Because the density of S is much lower than that of FeS_2, the red line is lower than the blue line in the case of the volumetric capacity.

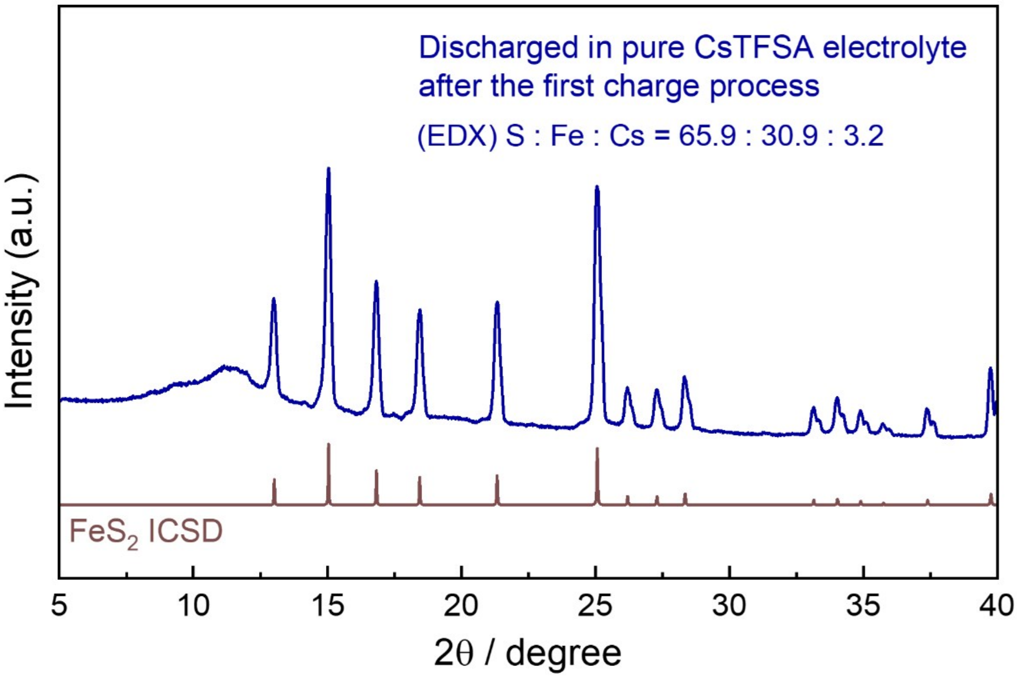

Figure S8. EDX and XRD results for the electrode that was discharged in pure CsTFSA electrolyte after the first charging process (i.e., Fe extraction from FeS_2). Although Cs was detected by EDX analysis, no sharp diffraction peaks were observed except for FeS_2. Instead, a halo peak appeared at around 10–12 degrees, indicating the formation of an amorphous phase. This is in strong contrast to the XRD profile of the electrode discharged in (Mg10/Cs90)TFSA, which exhibits obvious diffraction peaks from MgS.

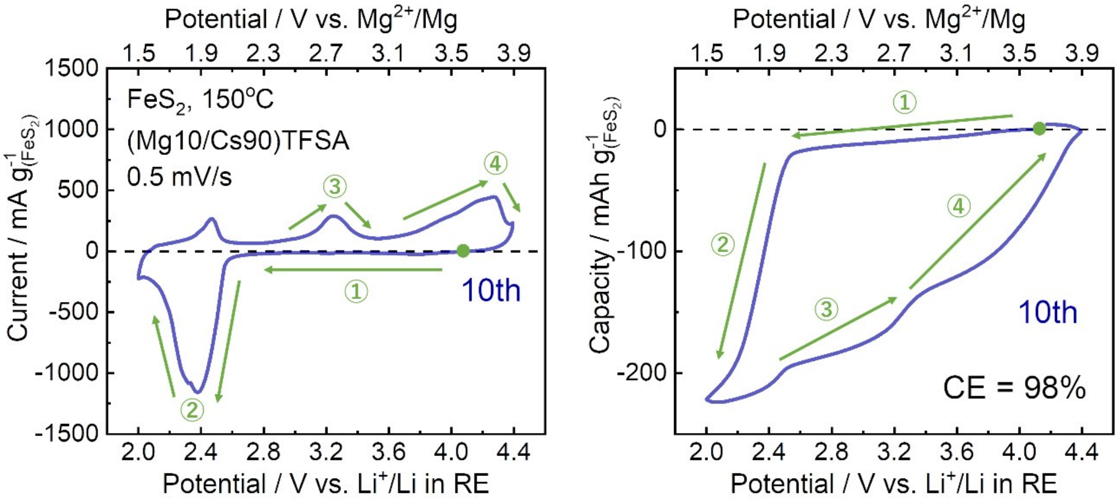

Figure S9. CV profile (left) and corresponding discharge/charge capacity (right) of the S/FeS_2 composite cathode in the electrolyte of (Mg10/Cs90)TFSA electrolyte at 150℃. The Coulombic efficiency was 98%, indicating high reversibility of magnesiation/demagnesiation.

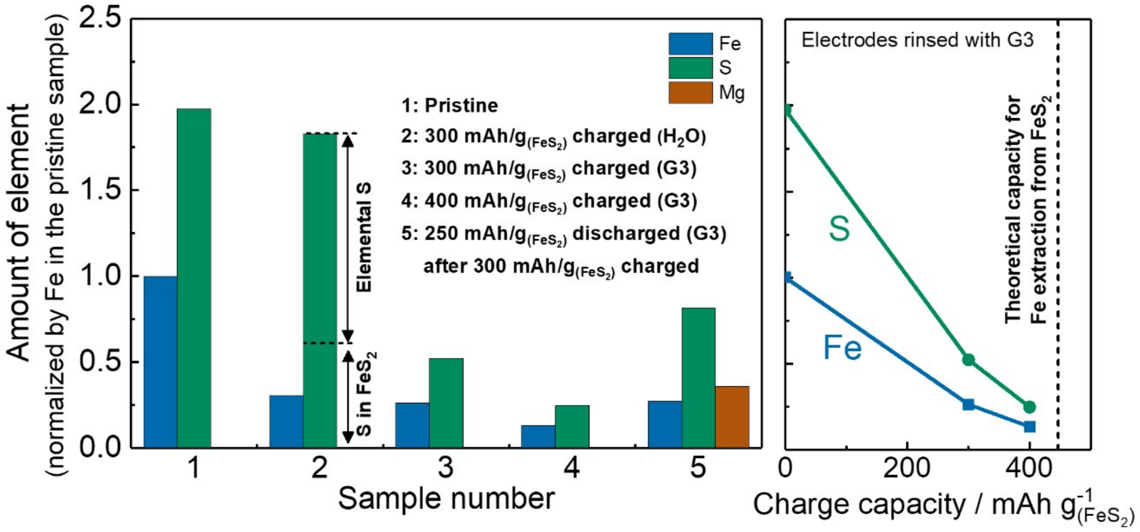

Figure S10. ICP results of the FeS_2 electrodes after charge/discharge. G3 and H_2O in parentheses indicate the solvents used for washing the electrodes. Note that elemental S is dissolved in G3 but not in H_2O, resulting in the difference between samples 2 and 3. As shown in the right panel, the decreasing rate of Fe and S for G3-washed samples matches well with the theoretical capacity for Fe extraction from FeS_2, indicating the high coulombic efficiency.

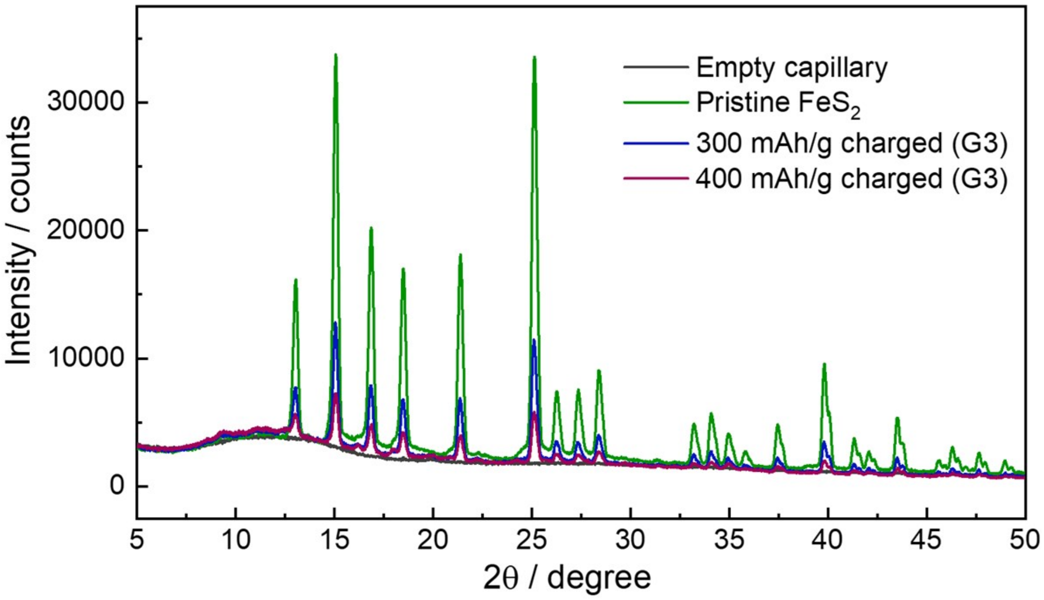

Figure S11. XRD profiles of the FeS_2 electrodes before/after the first charging process. Because the electrodes were rinsed with G3 as indicated in parentheses, the formed elemental S was eliminated. It was clearly seen that the intensity of diffraction peaks from FeS_2 was drastically lowered by charging, which is consistent with the result of ICP (see the right panel in Figure S10). This also supports that the reaction of eq 1 shown in the main text proceeds with high efficiency during the first charging process.

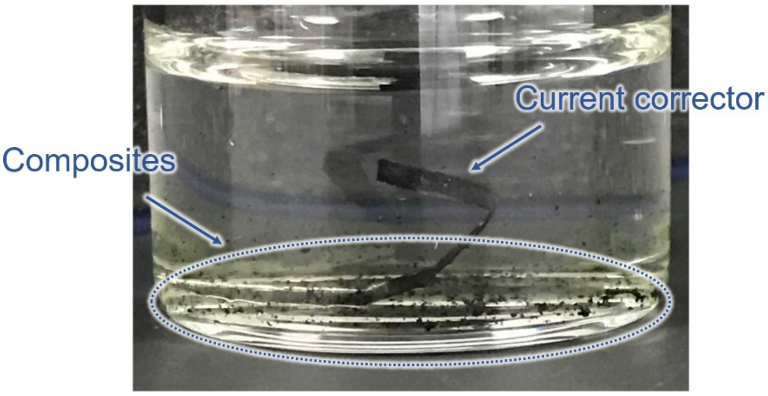

Figure S12. Digital photograph showing a discharged S/FeS_2 electrode rinsed with water. The discharged electrode reacted with water and the composites fell off from the Pt current corrector. The fine MgS particles formed in the discharging process would react with water because MgS is known to undergo hydrolysis.

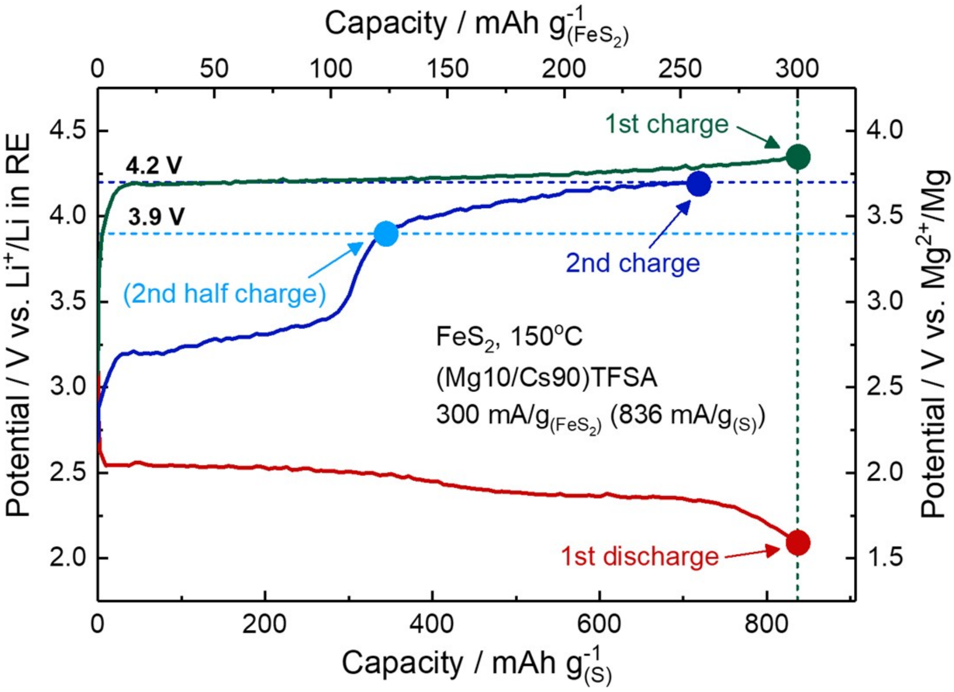

Figure S13. Galvanostatic charge/discharge profiles for preparing the samples used for XRD and XANES measurements, where the current density was set at 300 mA/$g_{(FeS2)}$. The charged and discharged electrodes were rinsed with G3 or water, respectively, before the XRD and XANES measurements.

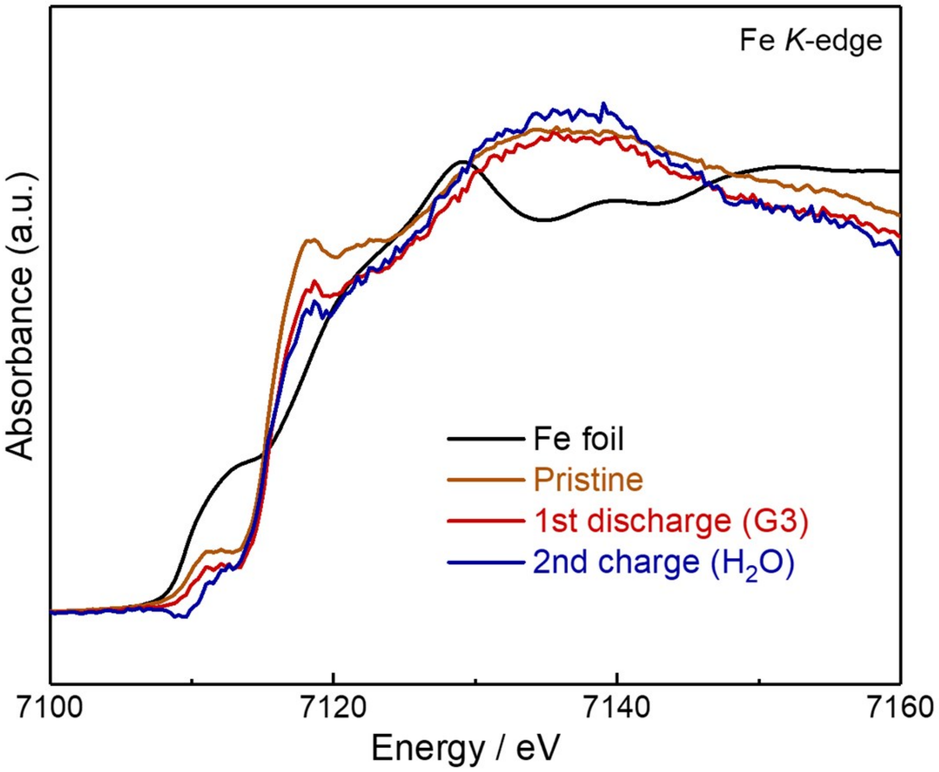

Figure S14. Fe *K*-edge XANES spectra for the S/FeS_2 composite electrodes after charge/discharge, together with that of a Fe foil (standard sample). G3 and H_2O in parentheses indicate the solvents used for washing the electrodes. The spectra were acquired by the fluorescence yielding mode followed by subtracting the XANES spectrum of the laminated Al film, which contains Fe as an impurity, from the measured spectra. The edge energy hardly changed after charge/discharge, indicating that the valence state of Fe was unchanged from 2+.

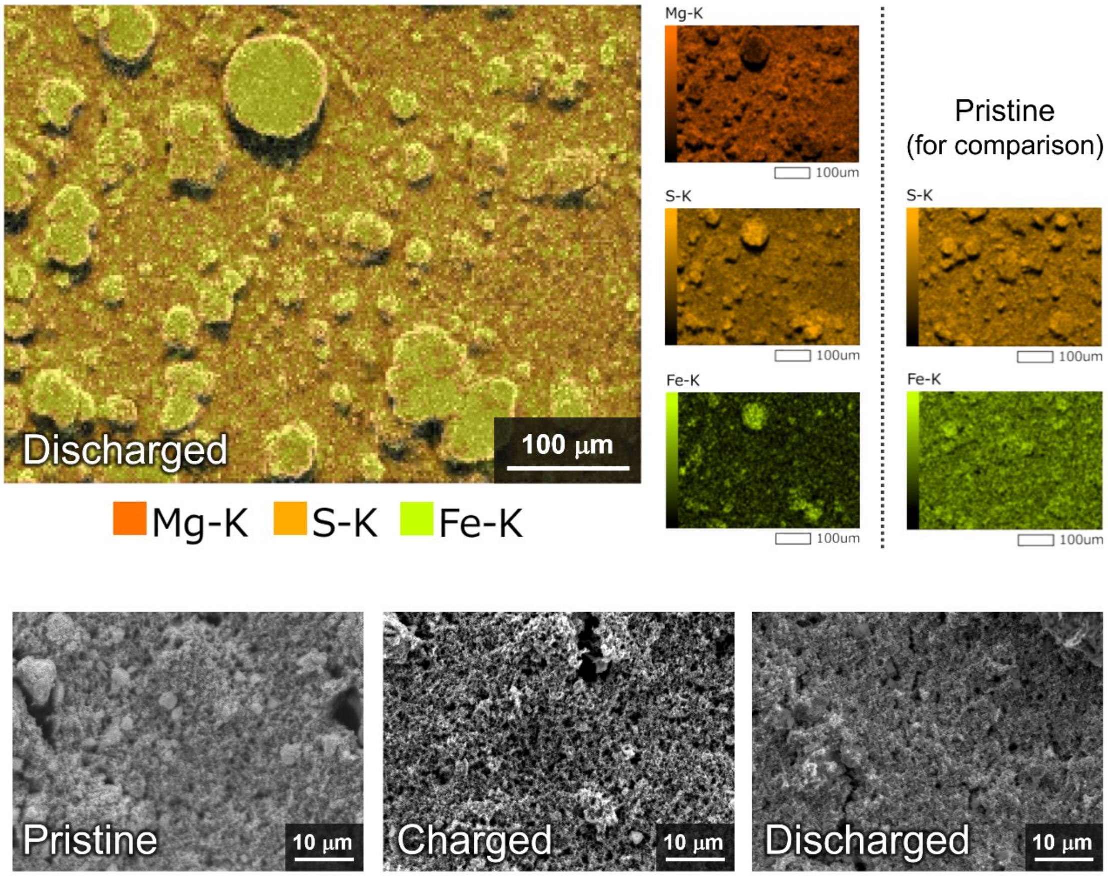

Figure S15. EDX mapping images for a discharged sample without FIB milling. EDX mapping for the pristine FeS_2 electrode is also shown for comparison. It is clearly seen that the Fe extraction from FeS_2 and the magnesiation of S occur heterogeneously, especially near the surface of coarse particles. SEM images for the pristine, charged, and discharged electrodes in the areas without coarse particles are also shown for reference. Charged and discharged electrodes were washed with G3.

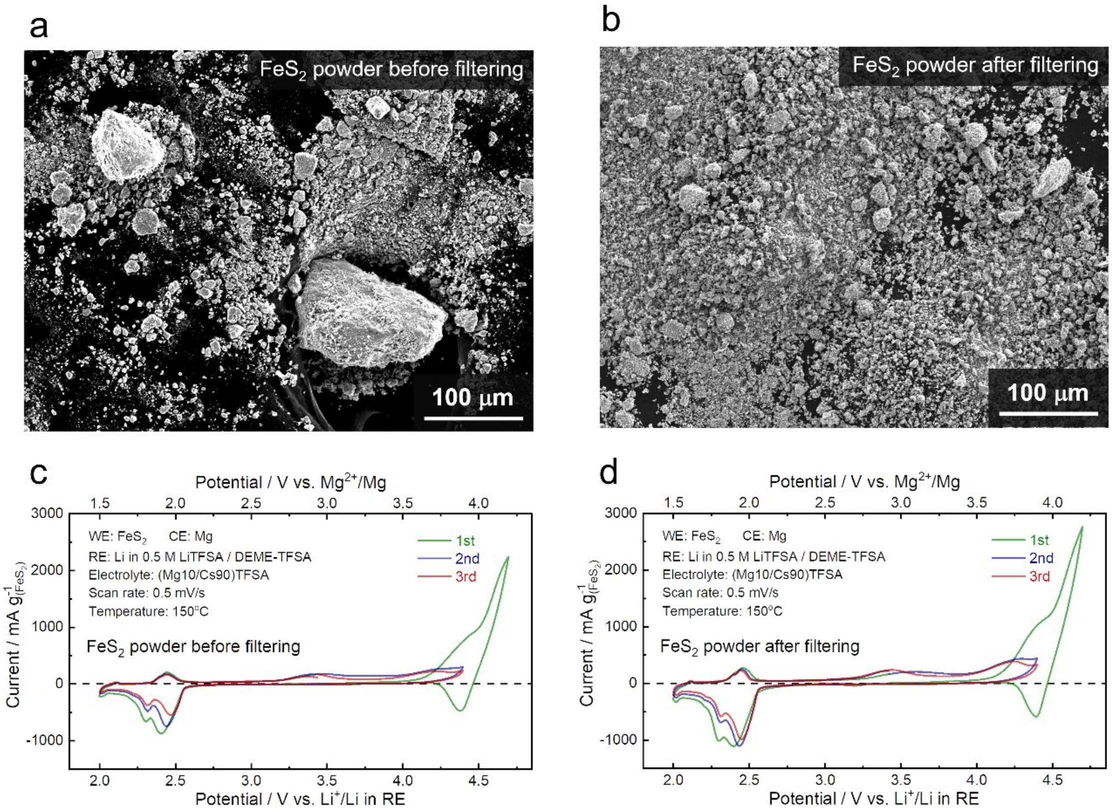

Figure S16. SEM images of FeS_2 powders (a) before and (b) after the filtering. It was clearly shown that large particles of ~100 µm were eliminated by filtering. CV profiles of FeS_2 powders (c) before and (d) after the filtering. The current density for FeS_2 powders before filtering is much lower than that of after filtering, indicating that the existence of large particles lowers the utility of FeS_2 because Fe extraction proceeds from the surface of particles.

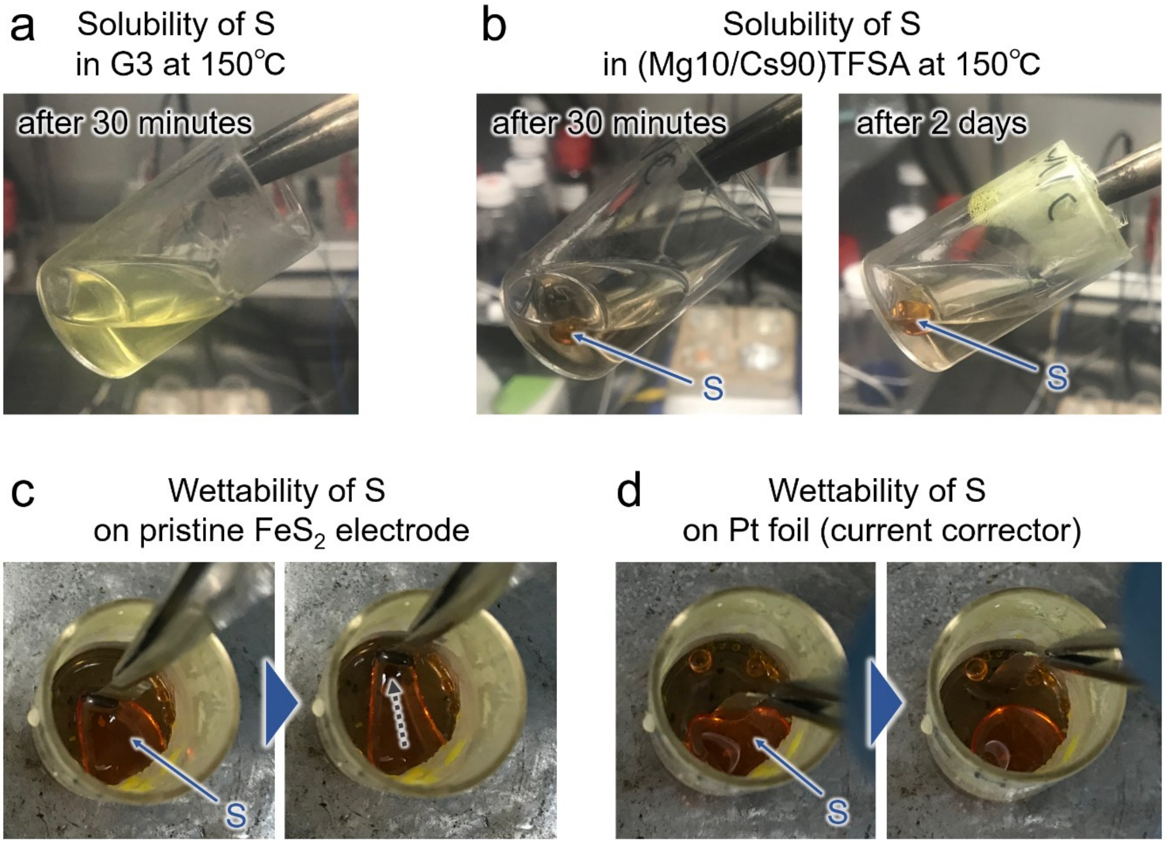

Figure S17. Digital photographs showing the solubility of elemental S in (a) G3 solvent and (b) (Mg10/Cs90)TFSA ionic liquid at 150°C. Although S easily dissolved in the G3 solvent, it formed a completely separated phase in the ionic liquid electrolyte even after 2 days. Digital photographs showing the wettability of elemental S on the (c) pristine FeS_2 electrode and (d) Pt foil in the (Mg10/Cs90)TFSA electrolyte at 150°C. Let the electrode touched to a liquid-S droplet (left) and then moved to upward (right). The droplet also moved following to the electrode, which indicates the high wettability of liquid S to the FeS_2 electrode. In contrast, such a behavior was not observed in the case of the Pt foil.

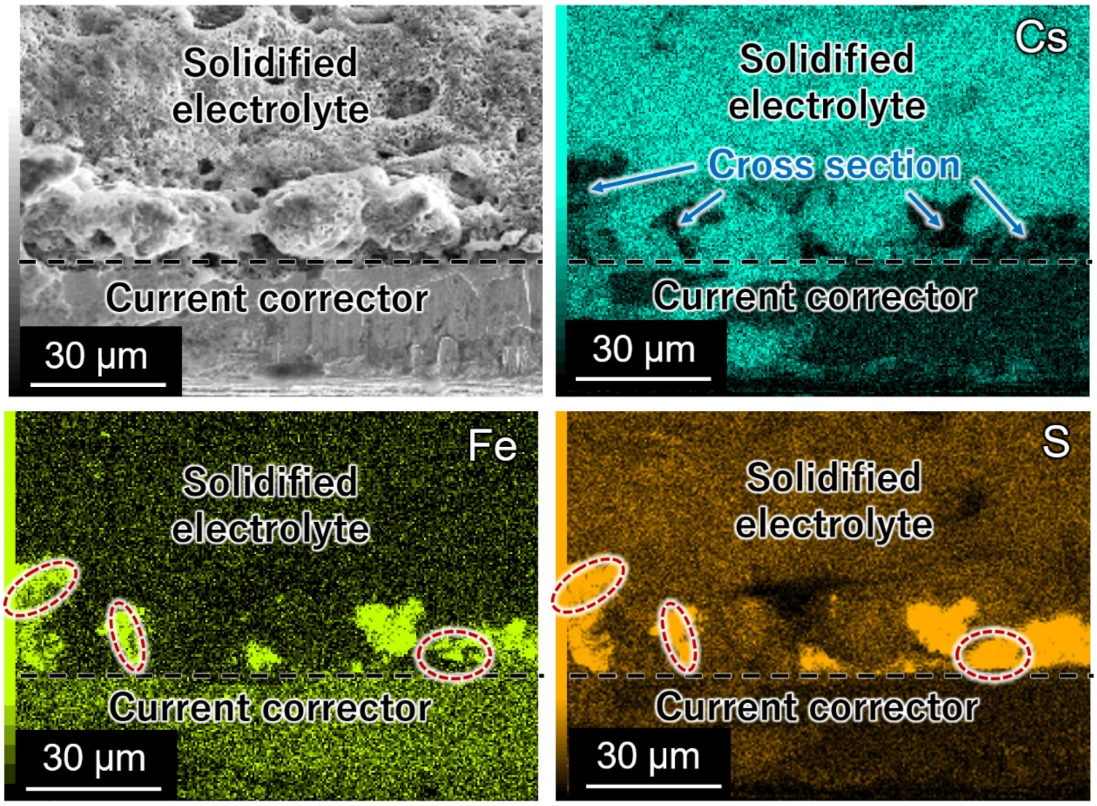

Figure S18. Cross-sectional SEM-EDX analysis for the FeS_2 electrode after the first charge. To preserve the morphology, the electrode was not washed with solvents; thus, most areas were covered with the solidified CsTFSA electrolyte. The electrode was cut by using a box cutter, not FIB, inside the grove box. The intensity of Fe was inhomogeneous due to the Fe extraction from the FeS_2 particles, while S was relatively homogeneously observed inside and around the porous FeS_2 particles especially at the points indicated by the red circles in the figure.

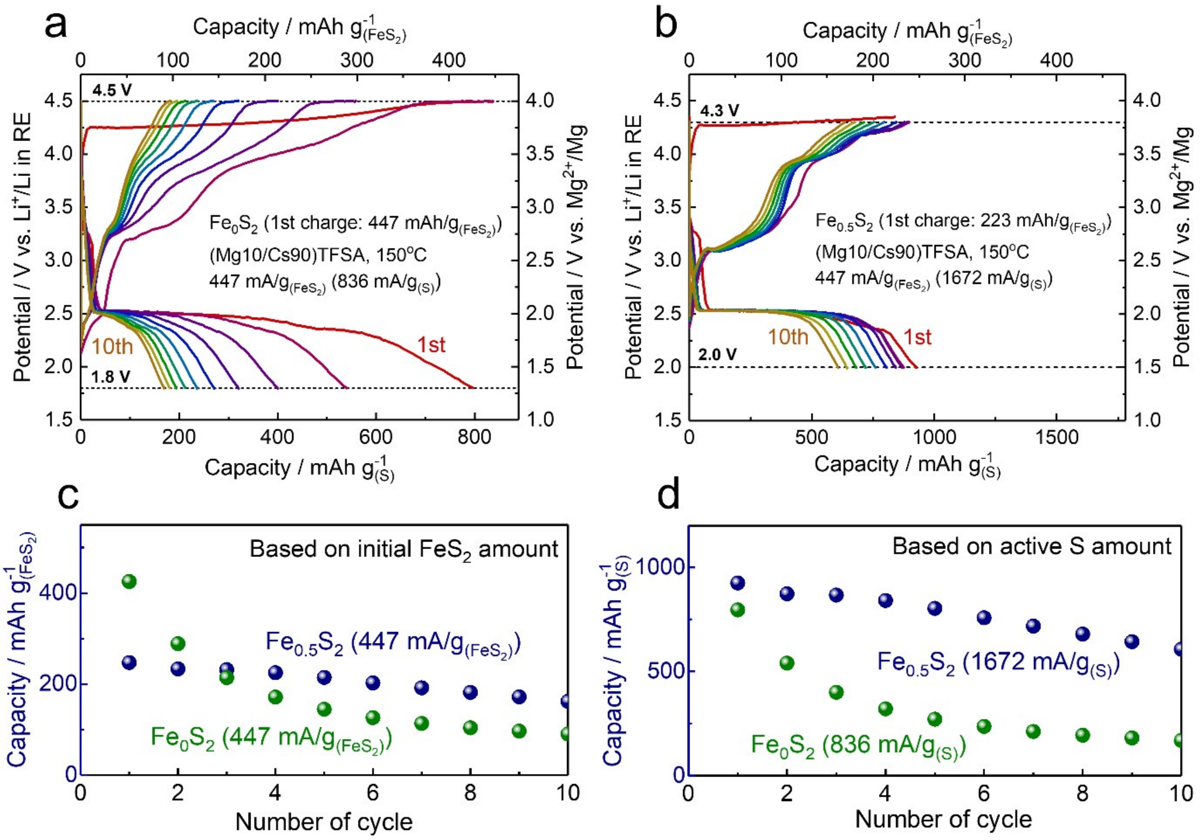

Figure S19. Charge/discharge curves of the S/FeS$_2$ cathodes with the first charge capacity of (a) 447 and (b) 223 mAh/g$_{(FeS2)}$, namely the nominal compositions of Fe$_0$S$_2$ and Fe$_{0.5}$S$_2$, respectively. The current density was set at 447 mA/g$_{(FeS2)}$ for the both cases (i.e., 863 and 1672 mAh/g$_{(S)}$, respectively, based on the amount of elemental S generated in the first charge). Note that the cut-off potentials were set so that the same capacity as the first charge (i.e., 447 and 223 mAh/g$_{(FeS2)}$) can be obtained in the subsequent cycles. Comparison of their capacity retentions on the basis of (c) initial FeS$_2$ and (d) active S amounts. Even based on the initial FeS$_2$ amount, the Fe$_{0.5}$S$_2$ electrode provided higher capacities compared to the case of the Fe$_0$S$_2$ electrode after cycles. Besides, a high rate capability of ~900 mAh/g$_{(S)}$ at 1672 mA/g$_{(S)}$ was stably achieved for the Fe$_{0.5}$S$_2$ in the first several cycles.

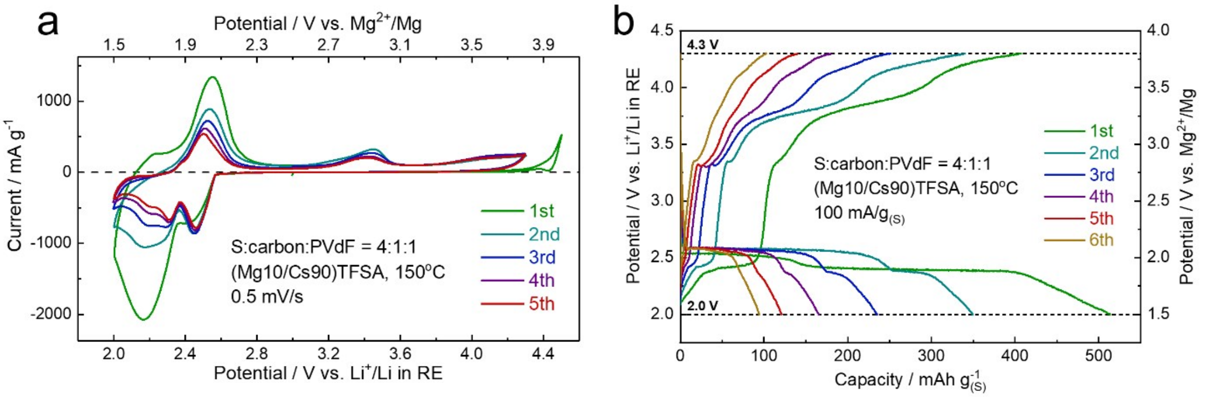

Figure S20. (a) CV and (b) galvanostatic discharge/charge profiles for S cathode prepared mixing in a weight ratio of S:carbon:PVdF = 4:1:1, where the galvanostatic cycling test was started from a discharge process. The peak positions in the CV profiles were similar to those for the FeS_2 electrode, whereas the reaction with Mg was suppressed compared to that with Cs probably due to kinetic reasons. The first discharge capacity in the galvanostatic test was ~500 mAh/g$_{(S)}$; however, it exhibited rapid capacity fading. The above result suggests that the FeS_2 frame plays an important role in improving the cyclability of the S/FeS_2 composite material.

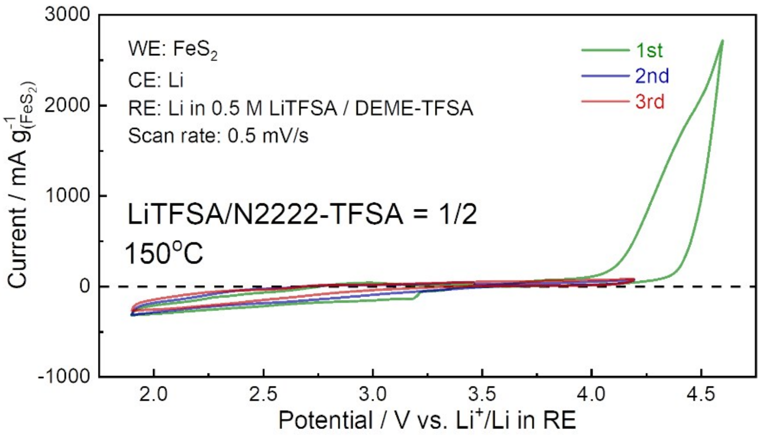

Figure S21. CV profiles of the FeS_2 electrode at 150°C in a Li-based ionic liquid electrolyte of LiTFSA/N2222-TFSA, where the molar fraction of LiTFSA is 33%. Although the Fe extraction from FeS_2 was indicated, it showed no obvious redox peaks in the subsequent cycles. Even when using a S/FeS_2 composite electrode prepared in CsTFSA electrolyte in advance, similar behavior was obtained. Thus, we consider that generated S was dissolved into the electrolytes, resulting in a rapid capacity fading. Because we used a beaker-type cell, the solubility of S into the electrolyte would be critical for electrochemical performance.

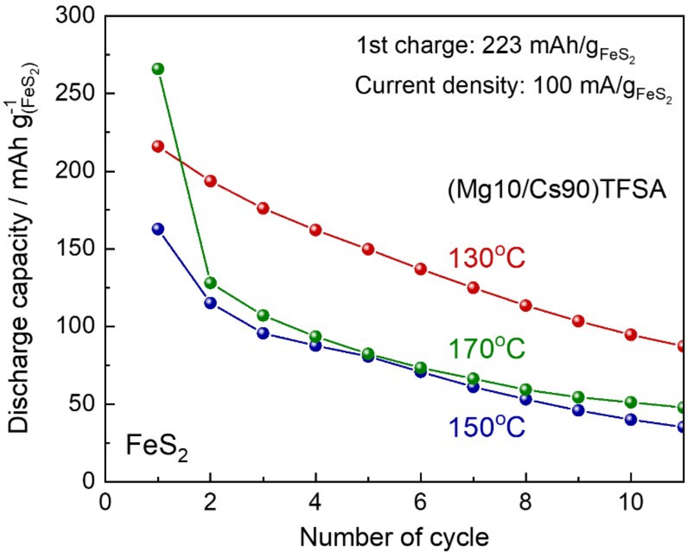

Figure S22. Cyclability of the S/FeS_2 cathode depending on the operating temperature. Considering the melting temperature and thermal stability of the electrolyte, we set the temperatures within 130–170°C. Although the first discharge capacity at 170°C is out of trend, the cell at 130°C showed relatively high capacities during the cycling test. This is probably because the dissolution and/or evaporation of S are suppressed by decreasing the operating temperature.

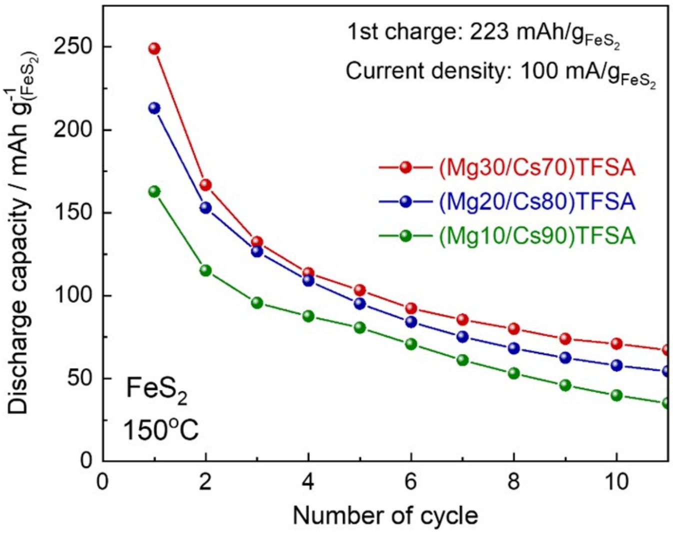

Figure S23. Cyclability of the S/FeS_2 cathode depending on the composition of the electrolyte. Because it was revealed by our ICP analysis that the dissolution of S proceeds faster in pure CsTFSA than in (Mg10/Cs90)TFSA, we increased the composition of $Mg(TFSA)_2$ in the electrolyte. The cyclability was increased with the increase in the concentration of Mg, suggesting that the dissolubility of S and/or polysulfides can be controlled by changing the composition of the molten salt electrolyte.

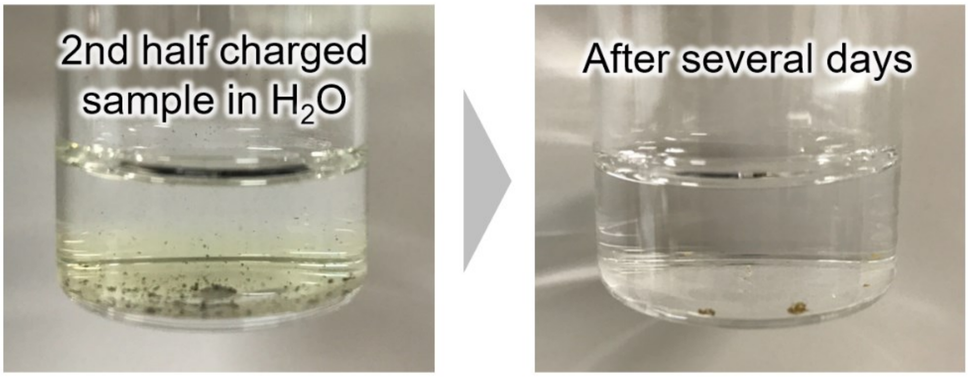

Figure S24. Digital photographs indicating the disproportional reaction of polysulfides in water. The yellow-colored water, which is used for rinsing the second half charged sample (see Figure S13), became colorless and an orange-colored solid product was formed after several days. This indicates that the polysulfides dissolved in water disproportionated to equilibrium products including elemental S insoluble to water. Indeed, the composition of the orange-colored solid product was confirmed to be basically S by EDX analysis.

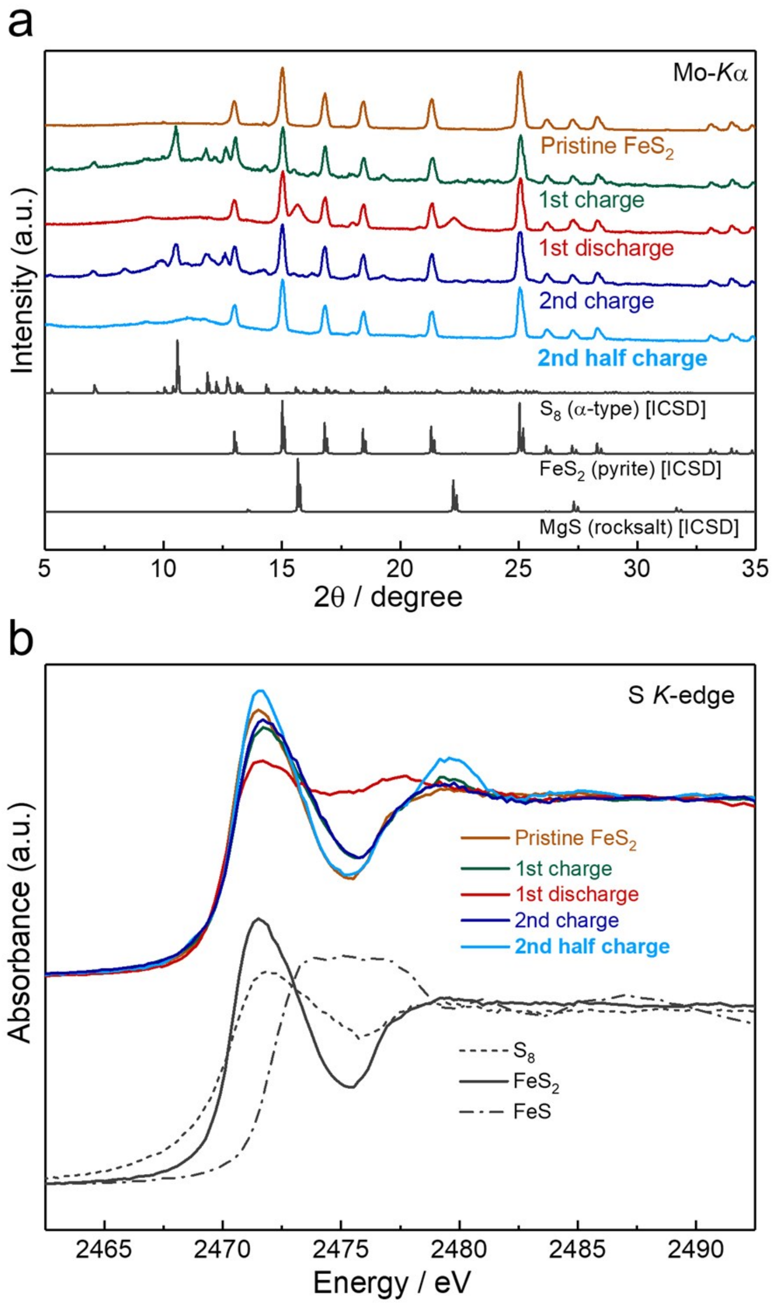

Figure S25. (a) XRD and (b) XANES spectra for the second "half" charged samples (i.e., charged up to 3.9 V vs. Li RE; see Figure S13), together with those for the other charged/discharged samples for comparison. The diffraction peaks for S_8 were not observed for the second half charged sample, which is in strong contrast with the first and second "full" charged samples (i.e., charged up to 4.2 V vs. Li RE). The XANES spectrum for the second half charged sample was very similar to that of the pristine FeS_2 sample, also indicating the absence of elemental S. A peak around 2480 eV can be attributed to the sulfate signal from TFSA anions according to a previous report [S2]. Note that the charged and discharged electrodes were washed with water and G3, respectively.

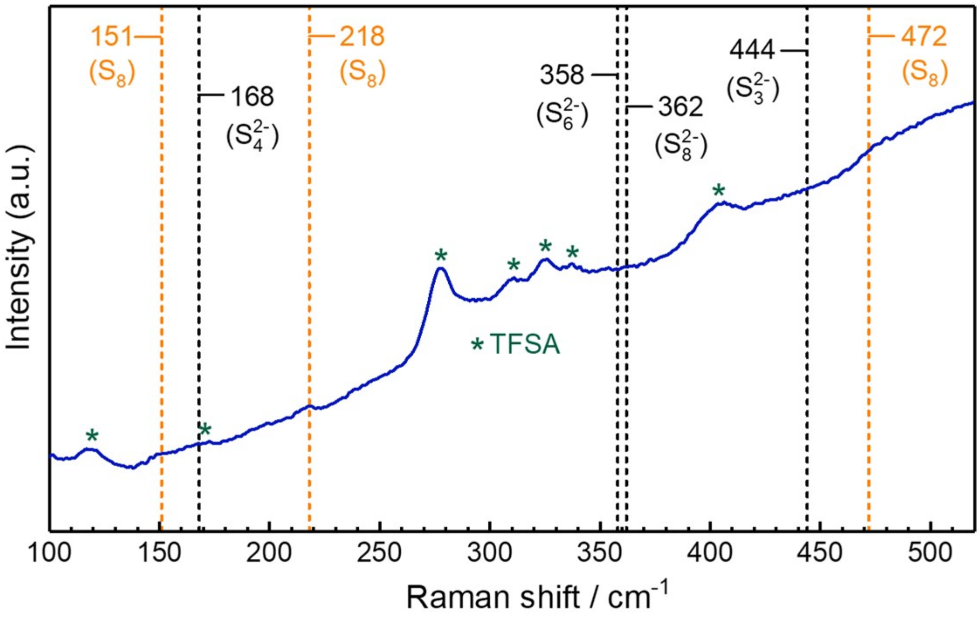

Figure S26. Raman spectrum for the THF solvent in which the second half charged sample was soaked. According to previous literature [S3], the strongest peaks for polysulfides of S_3^{2-}, S_4^{2-}, S_6^{2-}, and S_8^{2-} should appear in 444, 168, 358, and 362 cm^{-1}, respectively. Except for TFSA-related vibrational modes indicated by asterisks [S4], characteristic Raman bands were observed only for S_8 (151, 218, and 472 cm^{-1}), but not for S_3^{2-} (444 cm^{-1}), S_6^{2-} (358 cm^{-1}), and S_8^{2-} (362 cm^{-1}). Since the Raman band for S_4^{2-} (168 cm^{-1}) is overlapped with that of TFSA, it was difficult to distinguish them.

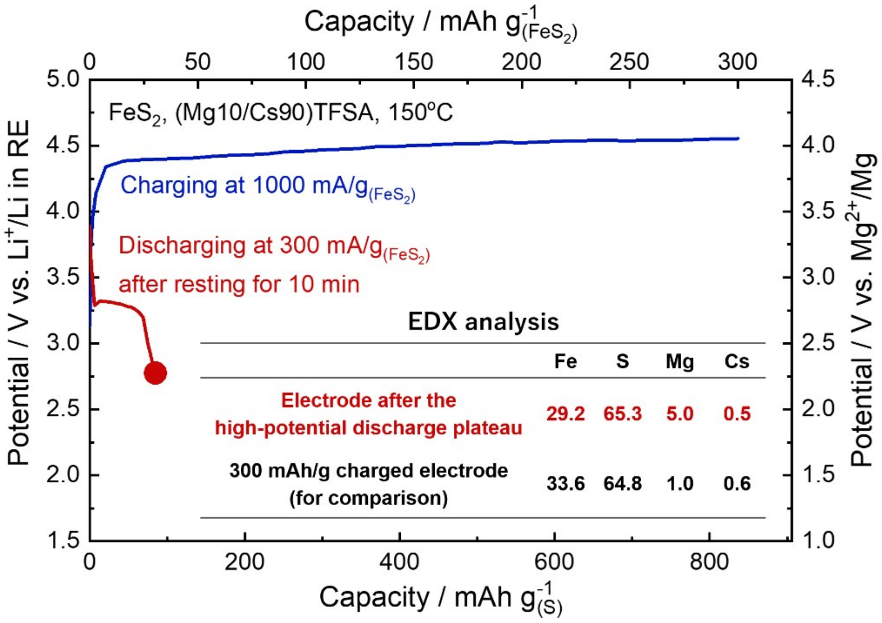

EDX analysis

	Fe	S	Mg	Cs
Electrode after the high-potential discharge plateau	29.2	65.3	5.0	0.5
300 mAh/g charged electrode (for comparison)	33.6	64.8	1.0	0.6

Figure S27. EDX analysis for the electrode discharged until the end of the high-potential plateau after high-rate charging at 1000 mA/$g_{(FeS2)}$. The electrode was washed with G3. It is clearly seen that the composition of Mg is increased compared to the charged electrode. The molar ratio of Mg/Fe is 0.171 (5.0/29.2), which is close to the theoretical value of 0.204 obtained by assuming that Fe^{2+} extraction from FeS_2 in charge and magnesiation in discharge proceed with 100% coulombic efficiency.

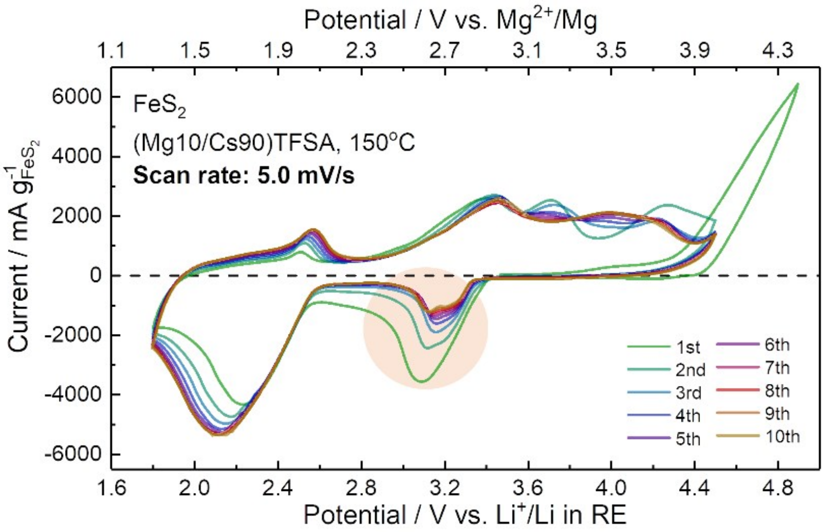

Figure S28. CVs of the FeS_2 cathode with PVdF binder at a relatively high scan rate of 5.0 mV/s. Cathodic peaks were also observed at relatively high potentials of ~3.2 V vs. Li RE, which were not observed in the CVs measured at 0.5 mV/s (see Figure 1d in the main text).

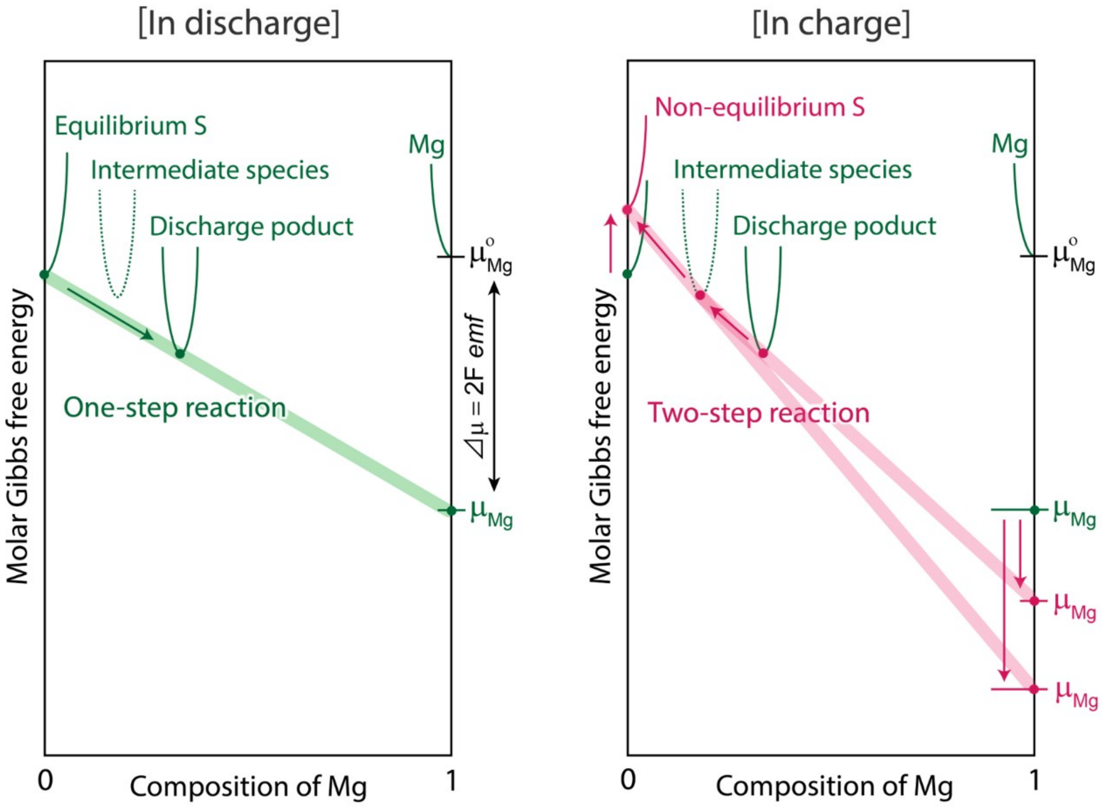

Figure S29. Schematic illustration for explaining the difference in the discharge and charge behavior observed in our experiments. In the discharging process, the discharge product can be formed directly from the equilibrium S by a one-step reaction. On the other hand, in the charging process, the formation of an intermediate species would be induced due to the relatively high chemical potential of non-equilibrium S formed during the charging process. This is a possible explanation for the behavior that two plateaus were observed only in the charging process when there is enough rest time between discharge and charge.

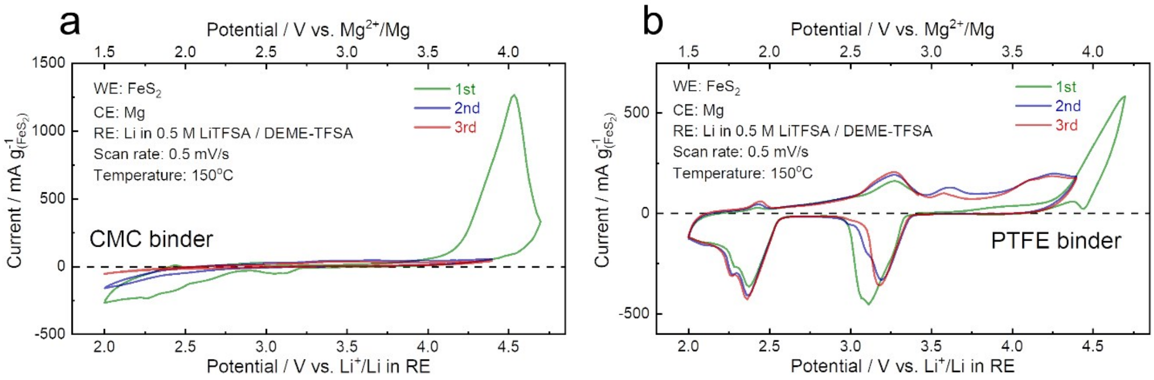

Figure S30. CV profiles of the FeS_2 electrodes prepared by using (a) CMC/water and (b) PTFE binders. Since the surface of FeS_2 particles can be easily oxidized, water used as the solvent for CMC binder would degrade some part of the particles in preparing the electrode. In fact, the first charge capacity was suddenly decreased before it reached the theoretical capacity in the case of using CMC binder. In addition, the high thermal stability of PTFE would be advantageous to achieve stable cyclability as demonstrated here.

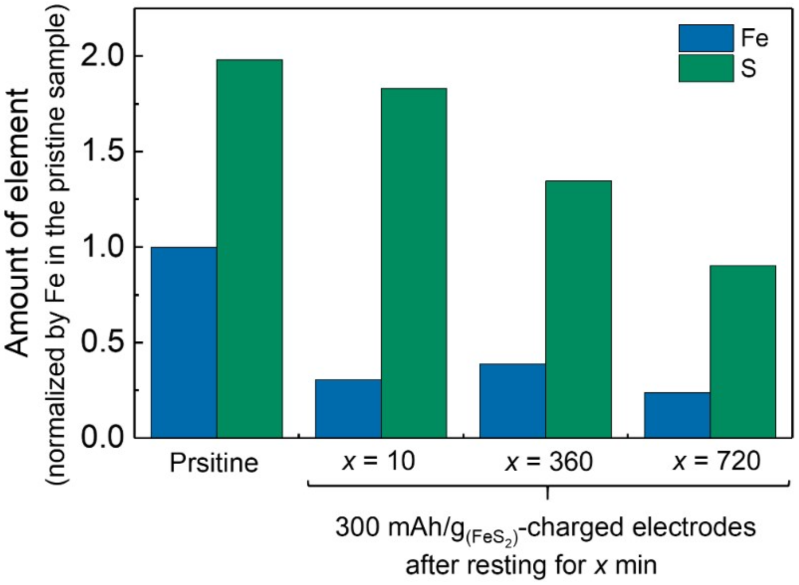

Figure S31. ICP results for 300 mAh/$g_{(FeS2)}$ charged samples with several resting time. The cathode and electrolyte used here were the FeS_2 electrode with PVdF binder and (Mg10/Cs90)TFSA ionic liquid at 150°C, respectively, and the electrodes were washed by water. The decrease in the amount of S was observed by resting the charged cathode in the electrolyte, suggesting that the generated S gradually dissolved into the electrolyte. This would be enhanced in the beaker-type call; however, it is expected that such a dissolution is suppressed in a practical setup with a small amount of electrolyte, owing to the low solubility of S into the TFSA-based ionic liquids.

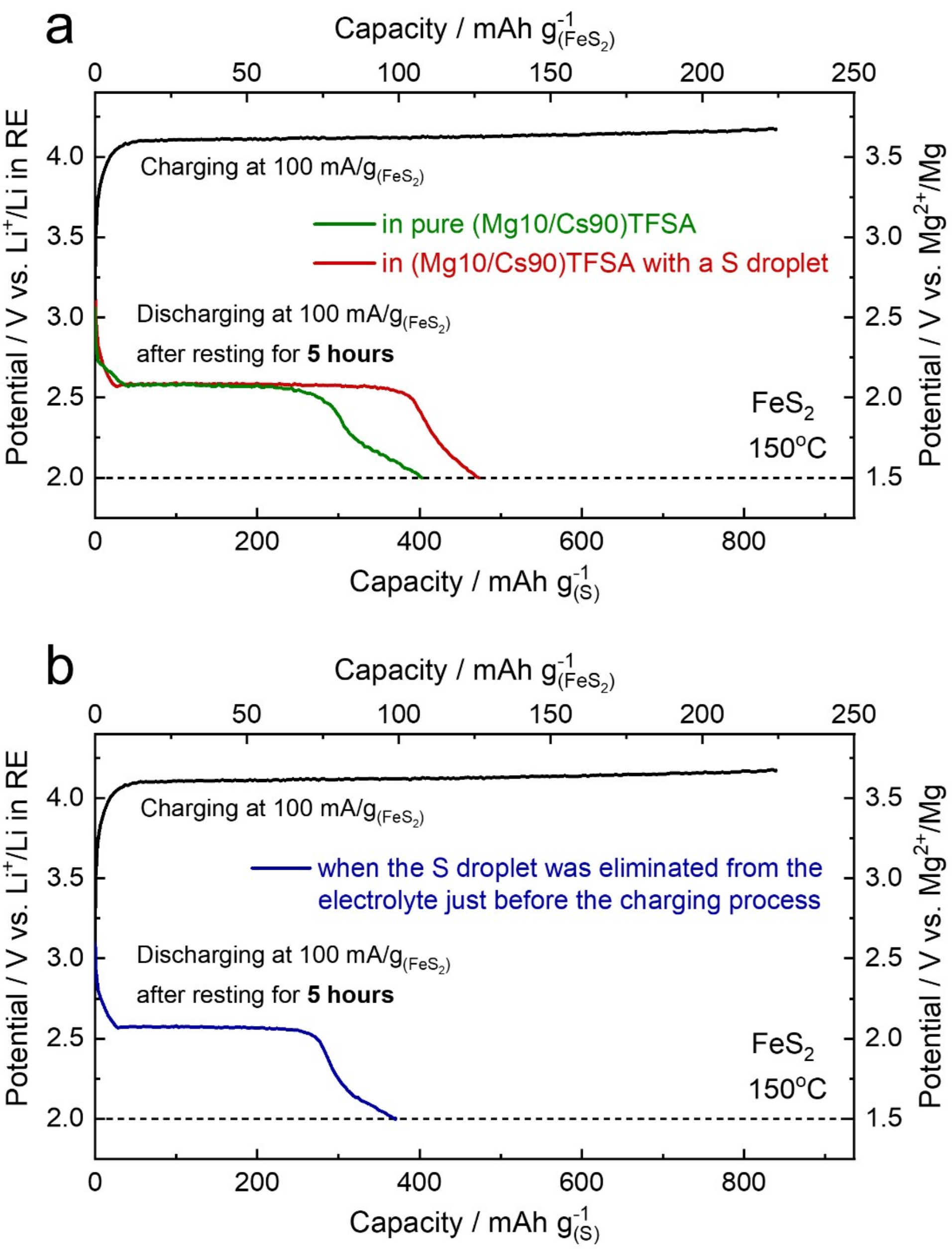

Figure S32. Charge/discharge curves of the FeS$_2$ electrode (a) with/without a S droplet for saturating the electrolyte and (b) when the S droplet was eliminated from the electrolyte just before the electrochemical measurement. A relatively high discharge capacity was obtained in the cell with a S droplet, indicating that suppressing the dissolution of S is important to enhance the capacity. Because the capacity was decreased when removing the S droplet just before the electrochemical measurement, we consider that the dissolved S was evaporated during the experiments, resulting in the loss of active materials.

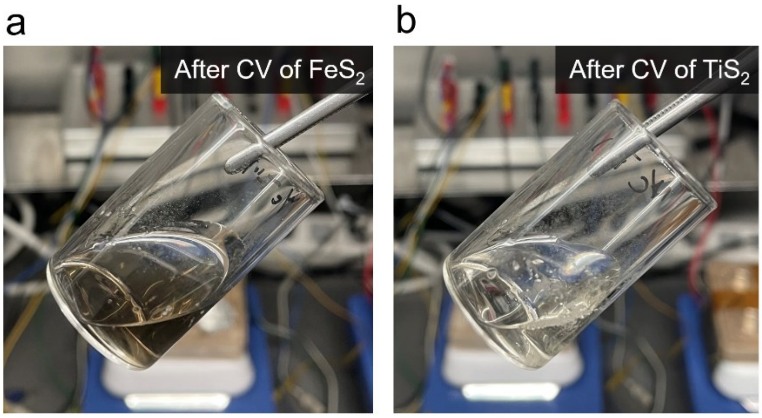

Figure S33. Digital photographs showing the (Mg10/Cs90)TFSA electrolytes after CVs of (a) FeS_2 and (b) TiS_2 electrodes. The color of electrolyte was brown after the CV measurement of FeS_2 electrode due to the extraction of Fe ions from FeS_2. On the other hand, it was colorless when using TiS_2 electrode. The molar ratio of Mg/Fe is over 200 in this setup, thus the magnesiation/demagnesiation reactions mainly proceed in discharge/charge as elucidated by various measurements in this study.

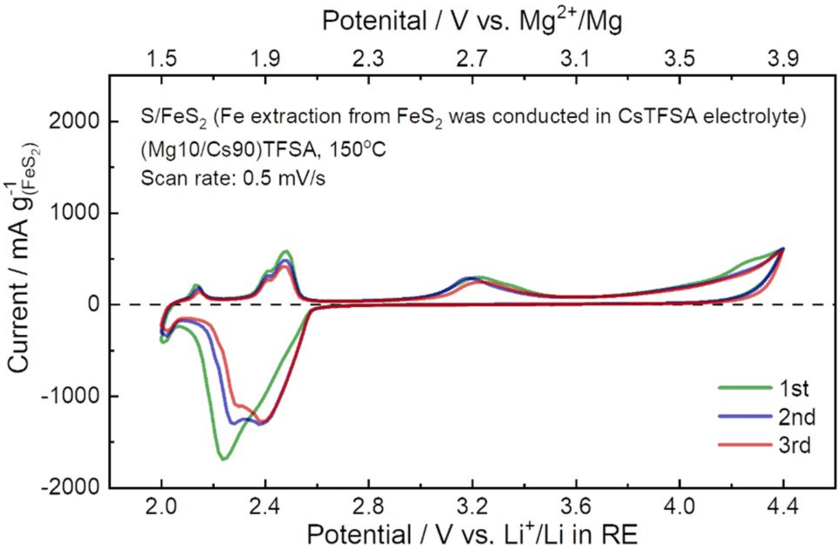

Figure S34. CV profiles of S/FeS_2 composite electrode that was prepared in pure CsTFSA electrolyte before the electrochemical measurement in the (Mg10/Cs90)TFSA electrolyte. The obtained behavior is very similar to the in-situ synthesized sample, e.g., Figure 1b in the manuscript. In practical use, the S/FeS_2 cathode should be prepared in advance as demonstrated here for preventing the contamination of cations such as Fe^{2+} in the electrolyte.

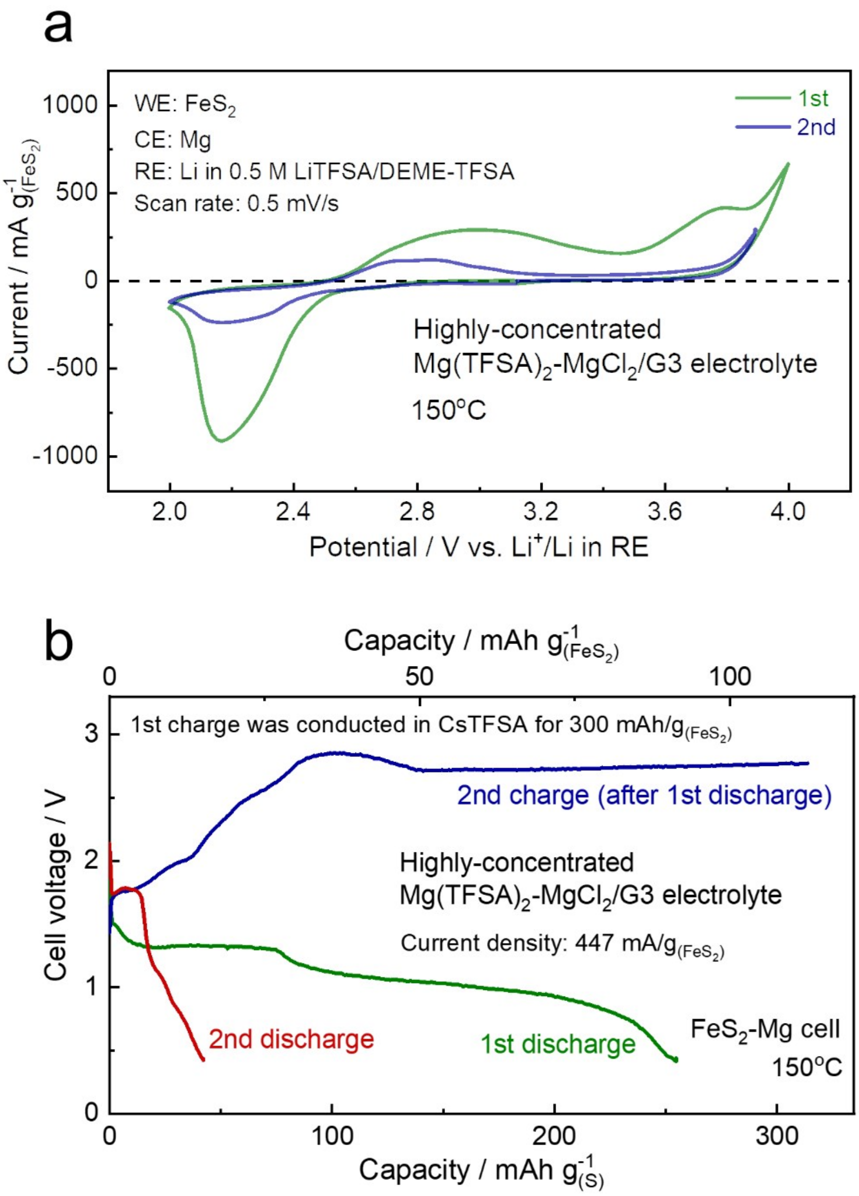

Figure S35. (a) CV profiles of the S/FeS_2 composite cathode in the electrolyte of a highly concentrated $Mg(TFSA)_2$–$MgCl_2$/G3 electrolyte, where the cathode material was prepared using the pure CsTFSA electrolyte before the CV measurement. Redox reactions indicating magnesiation/demagnesiation were clearly observed, although the cyclability was poor probably due to the dissolution of S into the G3-based electrolyte. (b) Discharge/charge curves of the S/FeS_2 | $Mg(TFSA)_2$–$MgCl_2$/G3 | Mg metal cell. The cell voltage of 1–1.5 V with a discharge capacity of 250 mAh/$g_{(S)}$ was obtained in the first discharge process.

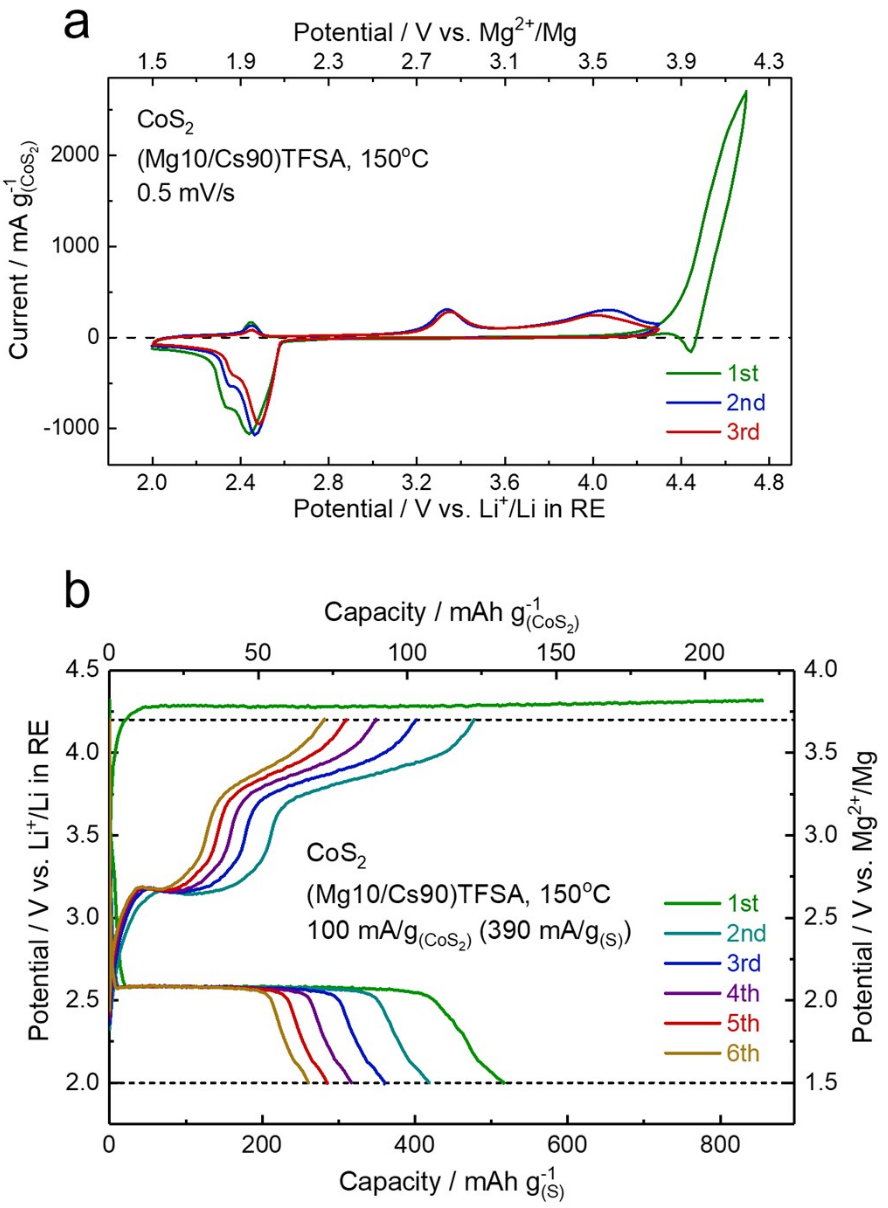

Figure S36. (a) CV and (b) galvanostatic charge/discharge profiles for the composite cathodes made from CoS_2 as the starting material. The obtained behavior was very similar to that of FeS_2. Flat plateaus were clearly observed even during the charging process in the galvanostatic test, suggesting slightly better kinetics compared to the case for the FeS_2 cathode.

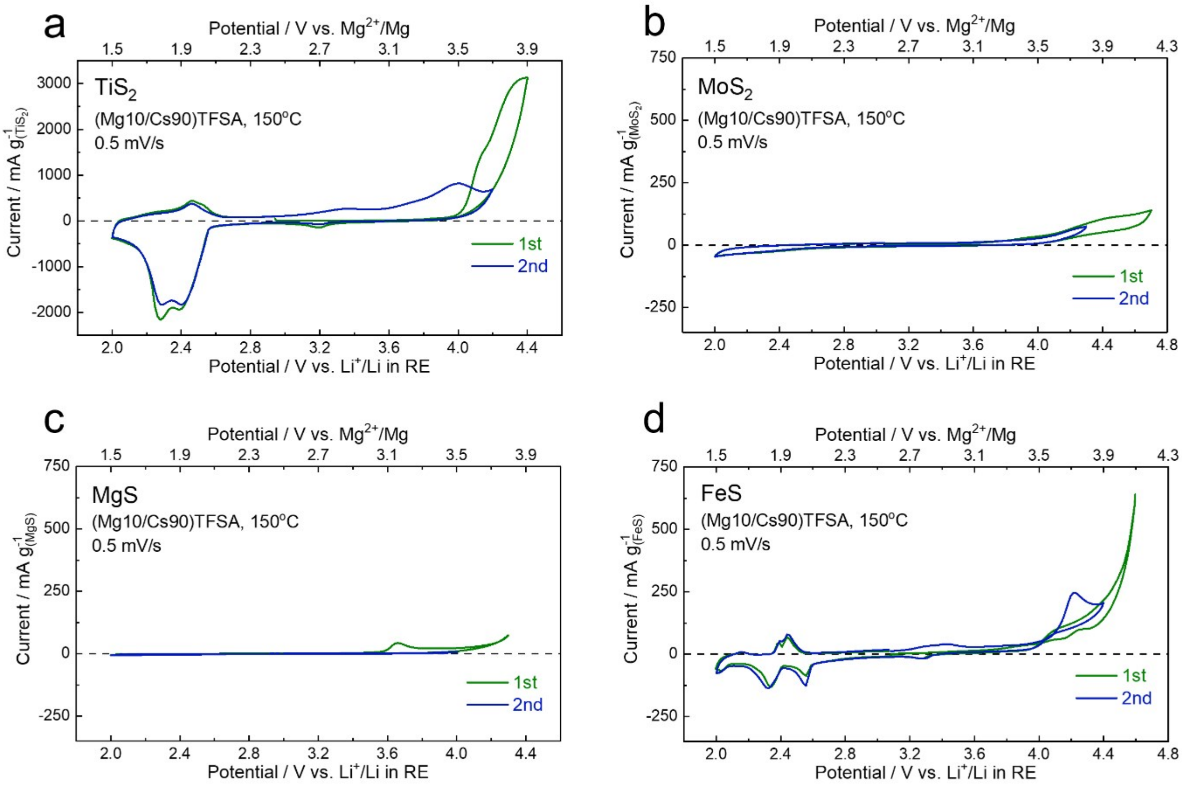

Figure S37. CV profiles of (a) TiS_2, (b) MoS_2, (c) MgS, and (d) FeS in the (Mg10/Cs90)TFSA electrolyte at 150°C. The obtained behavior of TiS_2 is very similar to that of FeS_2. As for MoS_2 and MgS, redox reactions corresponding to magnesiation/demagnesiation were hardly observed in the CV profiles. Although the cation extraction in the charge process was indicated for FeS, discharge capacities were relatively small compared to FeS_2.

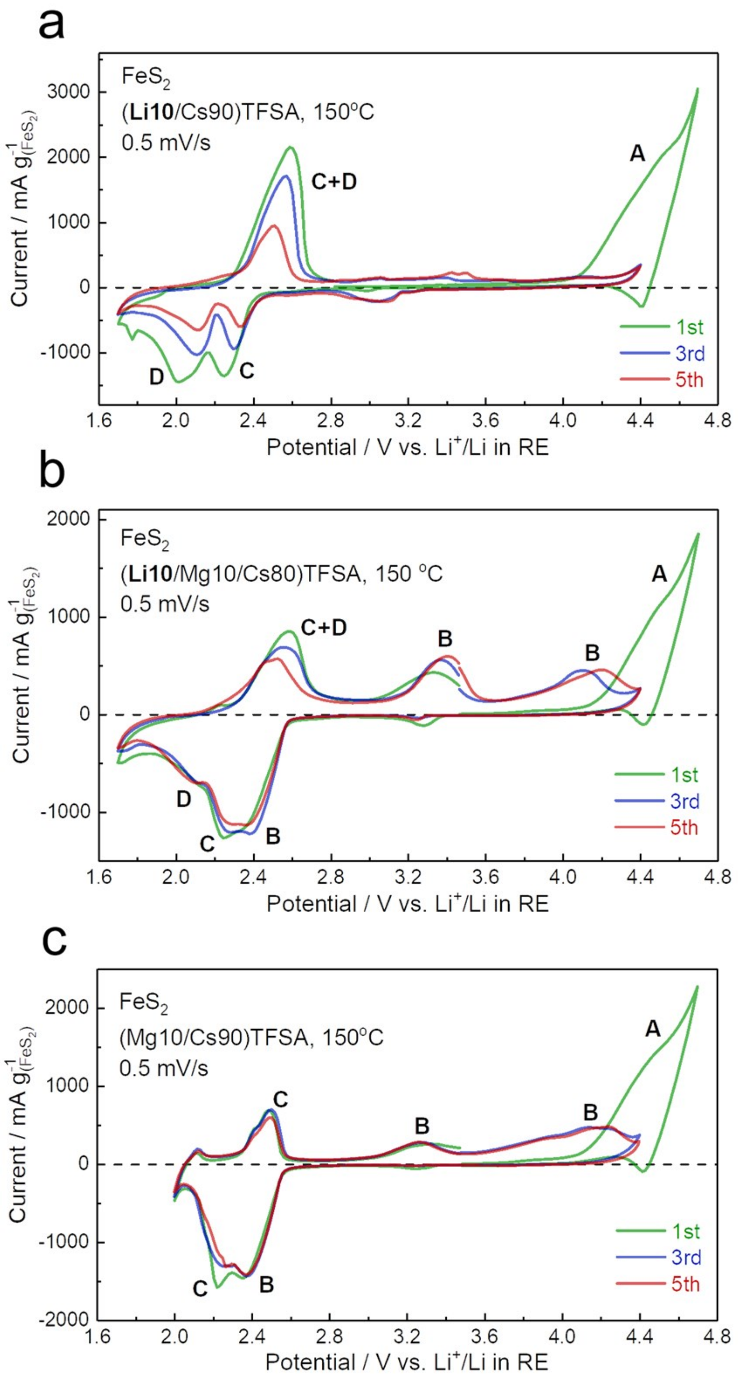

Figure S38. CV profiles for the FeS_2 cathode in the electrolytes of (a) (Li10/Cs90)TFSA, (b) (Li10/Mg10/Cs80)TFSA, and (c) (Mg10/Cs90)TFSA (for reference). The temperature was set at 150℃ for all experiments. Reactions A, B, and C correspond to the Fe extraction from FeS_2, the reactions of elemental S with Mg, and those with Cs, respectively, as mentioned in the main text. Reaction D was observed only for the Li-containing electrolytes; thus, it can be attributed to the reaction of S with Li. The redox potential for the reaction of S with Li is lower than that with Cs. This trend is consistent with a previous report [S5].

References:

[S1] Momma, K.; Izumi, F. VESTA 3 for three-dimensional visualization of crystal, volumetric and morphology data. *J. Appl. Cryst.* **2011**, 44, 1272−1276.

[S2] Robba, A.; Vizintin, A.; Bitenc, J.; Mali, G.; Arčon, I.; Kavčič, M.; Žitnik, M.; Bučar, K.; Aquilanti, G.; Martineau-Corcos, C.; Randon-Vitanova, A.; Dominko, R. Mechanistic study of magnesium−sulfur batteries. *Chem. Mater.* **2017**, 29, 9555−9564.

[S3] Hagen, M.; Schiffels, P.; Hammer, M.; Dörfler, S.; Tübke, J.; Hoffmann, M. J.; Althues, H.; Kaskel, S. In-situ Raman investigation of polysulfide formation in Li−S cells. *J. Electrochem. Soc.* **2013**, 160, A1205−A1214.

[S4] Capitani, F.; Trequattrini, F.; Palumbo, O.; Paolone, A.; Postorino, P. Phase transitions of PYR14-TFSI as a function of pressure and temperature: the competition between smaller volume and lower energy conformer. *J. Phys. Chem. B* **2016**, 120, 2921−2928.

[S5] Zou, Q.; Liang, Z.; Du, G.-Y.; Liu, C.-Y.; Li, E. Y.; Lu, Y.-C. Cation-directed selective polysulfide stabilization in alkali metal−sulfur batteries. *J. Am. Chem. Soc.* **2018**, 148, 10740−10748.